The Journal of Chemical Physics | ARTICLE | pubs.aip.org/aip/jcp

Quantifying fast structural relaxations in oxide V_2O_3 thin films

Cite as: J. Chem. Phys. 163, 084704 (2025); doi: 10.1063/5.0284153
Submitted: 5 June 2025 • Accepted: 31 July 2025 •
Published Online: 22 August 2025

View Online

Export Citation

CrossMark

P. Rajak,[1,2,3] S. K. Chaluvadi,[1,a)] S. Punathum Chalil,[1,2] F. Mazzola,[4] S. Passuti,[5] P. Orgiani,[1,b)] G. Rossi,[1,6] and R. Ciancio[5,c)]

AFFILIATIONS

[1] CNR-IOM Istituto Officina dei Materiali, 34149 Trieste, Italy
[2] International Centre for Theoretical Physics (ICTP), 34151 Trieste, Italy
[3] Department of Physics, Balurghat College, Dakshin Dinajpur, West Bengal 733101, India
[4] CNR-SPIN UoS Napoli, 80125 Napoli, Italy
[5] AREA Science Park, 34149 Trieste, Italy
[6] Department of Physics, University of Milano, 20133 Milano, Italy

Note: This paper is part of the JCP Special Topic, Annabella Selloni Festschrift.
[a)] **Author to whom correspondence should be addressed:** sandeepkumar.chaluvadi@cnr.it
[b)] **Electronic mail:** pasquale.orgiani@cnr.it
[c)] **Electronic mail:** regina.ciancio@areasciencepark.it

22 August 2025 17:04:14

ABSTRACT

Vanadium sesquioxide (V_2O_3) attracts considerable interest due to its high technological potential in many devices for resistive switching, energy storage, catalysis, etc. To harness the full potential of these materials in functional devices, it is crucial to understand the dynamics of the structural relaxation process exhibited when grown in thin film form. Here, we present a comprehensive study on the fast-structural relaxation phenomenon observed in V_2O_3 thin films grown by the pulsed laser deposition technique using a Nd:YAG pulsed infrared laser source. To assess the quality of the interface, structural change, and chemical composition, a quantitative analysis of the transmission electron microscopy images was conducted. Strain analysis reveals that structural relaxation in V_2O_3 thin films occurs rapidly within the initial ~4 nm from the film–substrate interface. This relaxation mechanism involves the formation of dislocations near the interface. These findings suggest that enhanced strain coupling at the film–substrate interface contributes to the observed relaxation behavior, underscoring the sensitivity of V_2O_3's strongly correlated metallic phase to crystalline defects and structural disorder. Understanding these interfacial relaxation dynamics is critical for the design and optimization of V_2O_3-based functional devices.

© 2025 Author(s). All article content, except where otherwise noted, is licensed under a Creative Commons Attribution (CC BY) license (https://creativecommons.org/licenses/by/4.0/). https://doi.org/10.1063/5.0284153

I. INTRODUCTION

Oxide materials have garnered significant attention for electronic and sensing applications.[1–9] Among these, vanadium sesquioxide (V_2O_3) stands out due to its well-known metal–insulator transition (MIT)[10,11] in response to slight variations in temperature or external stimuli.[12,13] At room temperature, bulk V_2O_3 is a metallic paramagnet.[14] Upon cooling, it undergoes a first-order phase transition from a corundum structure with rhombohedral symmetry ($R\bar{3}c$ space group) to a monoclinic structure (I2/a).[15,16] Such a transition occurs within a narrow temperature range (~160 K) and is characterized by a change in the electrical conductivity of more than seven orders of magnitude.[17]

V_2O_3 thin films also exhibit this transition and are promising candidates for integration into multilayered functional heterostructures, with potential applications in planar devices such as piezoelectronics[18] and field effect transistors.[19] However, unlike bulk materials, the phase transition in V_2O_3 thin films can be significantly influenced by epitaxial strain,[20] oxygen defects,[21] dimensionality,[16] and structural disorder.[22] The reported electronic and structural properties of V_2O_3 films vary widely, especially for ultra-thin films, due to the strong influence of the film/substrate interface.[23–25]

Therefore, it is crucial to develop robust growth methods for producing high-quality V_2O_3 thin films with atomically sharp oxide–oxide interfaces and to understand how the substrate-induced strain and interfacial defects affect the correlated electronic properties.[16,26]

In this study, we have investigated the structural properties of V_2O_3 thin films as thin as a few nanometers. Among the various techniques used for the growth of V_2O_3 thin films, such as magnetron sputtering,[27,28] atomic layer deposition,[29] molecular beam epitaxy,[30,31] and chemical solution deposition,[32] we here present results on thin films grown by the pulsed laser deposition (PLD) technique,[26,33] which allows controlling the growth of diverse materials at the level of single atomic layers and synthesizing them within a single-run deposition process with high control of structure, stoichiometry, and termination.[34]

X-ray diffraction (XRD) analyses have confirmed the successful fabrication of high-crystalline quality V_2O_3 thin films, while microstructures at the surface of the thin films have been assessed by Scanning Electron Microscopy (SEM). To characterize the morphology, structure, and composition of materials with atomic resolution, high-resolution transmission electron microscopy (HRTEM) has been employed.[35,36] HRTEM indeed provides valuable insight into the growth mechanisms, defects, and interface properties of the films, enabling a better understanding of their behavior and potential applications. Furthermore, geometrical phase analysis (GPA) has assessed the strain evolution within the V_2O_3 films. In the ultrathin film limit, the full relaxation of the V_2O_3 structure has been proved to occur through misfit dislocations[17] and is accompanied by residual strains associated with these dislocations until the film reaches bulk-like V_2O_3. The combination of these techniques provides a comprehensive insight into the structural properties of the films and their underlying physical characteristics.

II. RESULTS

Epitaxial V_2O_3 films were fabricated with thicknesses ranging from 15 nm down to 5 nm. Films were grown on c-plane (0001)-oriented Al_2O_3 sapphire, which shares V_2O_3's rhombohedral $R\bar{3}c$ crystal symmetry and has a ~4% smaller in-plane lattice constant (V_2O_3 unit cell, a = 4.9776 Å and c = 13.9647 Å;[37] Al_2O_3 unit cell, a = 4.7605 Å and c = 12.9956 Å[38]).

A. Surface morphology probed by SEM

Surface morphologies of V_2O_3 thin films with varying thicknesses were characterized using SEM. Figure 1 presents FEG-SEM images that offer a detailed view of the microstructural characteristics of highly textured V_2O_3 films. All of the films display smooth surfaces without droplets or cracks, as illustrated in Figs. 1(a)–1(c). Upon further examination at higher magnifications, distinct differences in surface morphology are evident among the samples. Films with lower thicknesses, specifically 5 and 8 nm, exhibit similar grainy surface textures [Figs. 1(d) and 1(e)], while the film with a thickness of 15 nm shows a noticeably smoother surface [Fig. 1(f)]. The grainy morphology observed in the thinner films is attributed to the Volmer–Weber type island growth mode.[23] As the film thickness increases, these islands coalesce, thus resulting in the decrease of screw-type island formation, as evidenced by the smoother surface of the 15 nm thick film.

B. X-ray diffraction analysis

The symmetrical θ–2θ scan of the V_2O_3 thin film grown on a sapphire Al_2O_3 substrate revealed a single-crystalline phase [Fig. 2(a)]. The diffraction pattern displayed a prominent peak corresponding to (006*l*) orientations, indicating that the film is highly oriented along the *c*-axis and confirming rhombohedral $R\bar{3}c$ crystal symmetry. The absence of additional peaks confirmed the lack of secondary phases or misoriented grains. The out-of-plane lattice parameter *c* was determined from the (006) Bragg diffraction peak and found to be 13.97 ± 0.01 Å, which corresponds to the bulk lattice constant.[37] To evaluate possible strain states of the V_2O_3 thin films, reciprocal space maps were performed around the (1010) asymmetric reflection of the film and the substrate [Fig. 2(b)]. The analysis performed on a 10-nm thick film revealed that the Q_x vectors of the film and the substrate do not align, confirming that V_2O_3 is not strained with respect to the Al_2O_3 substrate. The significant lattice mismatch (≈4%) between the film and substrate promotes relaxation of the film within a few nanometers of thickness through the formation of dislocations, as discussed in the Transmission electron microscope experiments section (Sec. II C). Finally, the thickness as well as the surface roughness of the V_2O_3 films were determined using low-angle x-ray reflectivity (XRR), as presented in Fig. 2(c).

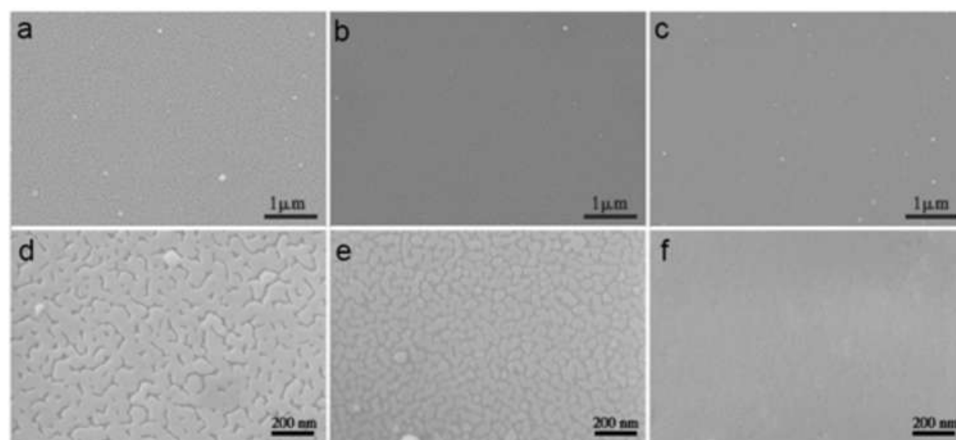

FIG. 1. SEM surface images of V_2O_3/Al_2O_3 heterostructure with varying V_2O_3 film thickness: [(a) and (d)] 5 nm, [(b) and (e)] 8 nm, and [(c) and (f)] 15 nm, taken at low and high magnifications, respectively.

22 August 2025 17:04:14

© Author(s) 2025

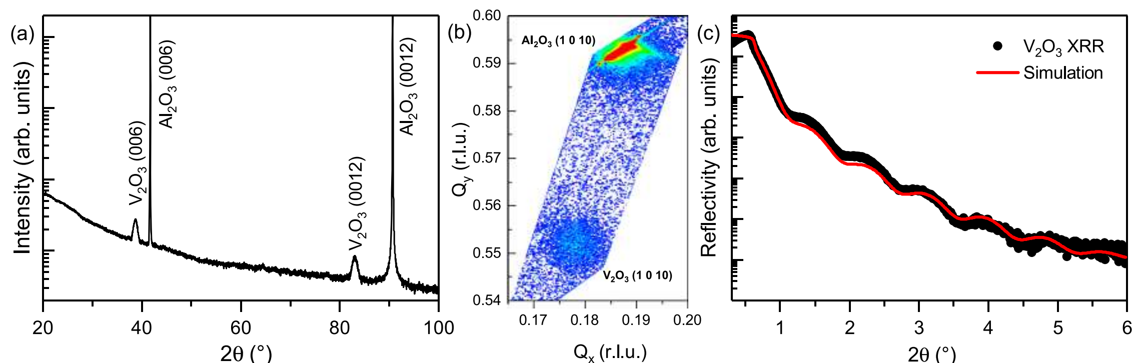

FIG. 2. (a) Long-range θ–2θ scan, (b) reciprocal space map around the film/substrate's (1010) asymmetric reflection, and (c) low-angle x-ray reflectivity of a 10 nm-thick V_2O_3 film. The red solid line in panel (c) indicates the simulated curve of the XRR data.

Numerical simulations of the XRR data [red solid curve in Fig. 2(c)] were performed using the AMASS software by Malvern. The fitting results revealed a film thickness of 10 nm and a surface roughness of about 0.6 nm, which corresponds approximately to the height of a half single unit cell of V_2O_3.

C. Transmission electron microscope experiments

TEM studies were conducted on the V_2O_3 thin film to investigate the morphology, local structure, crystalline quality, and in-plane orientation at the nanoscale. A slightly thicker film of 15 nm was chosen to visualize both the interfacial region and the bulk-like regions while minimizing the effects of surface degradation.[33] Figure 3(a) shows a representative low-magnification cross-sectional bright-field TEM image of the V_2O_3/Al_2O_3 heterostructure. The image demonstrates the uniform growth of the film, exhibiting a smooth surface structure without any significant defects.

To gain a deeper understanding of the crystalline structure and interface quality, HRTEM experiments were also performed. The HRTEM image in Fig. 3(b) shows the highly crystalline nature of the film, along with atomically flat interfaces with the substrate. Figures 3(c) and 3(d) display the fast Fourier transform (FFT) patterns of the V_2O_3 film and Al_2O_3 substrate, revealing distinct spot-diffraction patterns indicating their single crystalline characteristics. Moreover, the FFT patterns can be safely assigned to the corundum-phase structure. From the HRTEM image [Fig. 3(b)] and the FFT pattern, the interplanar distances are measured as 0.23 and 0.25 nm,

22 August 2025 17:04:14

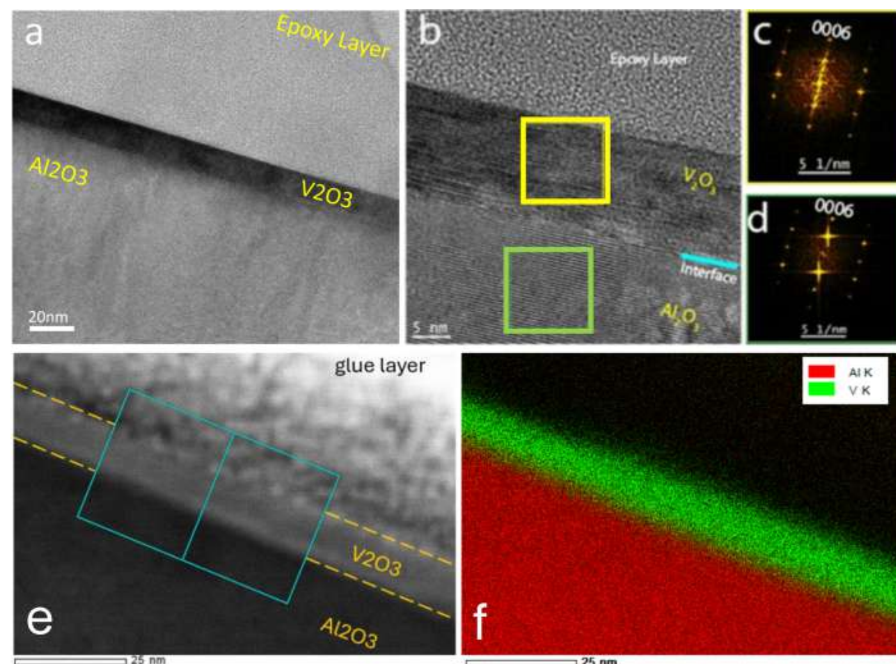

FIG. 3. Upper panel: (a) A low-magnification TEM image of the cross-sectional sample of 15 nm thick V_2O_3/Al_2O_3 heterostructures. (b) A HRTEM image of the heterostructure showing the interface along the $[\bar{1}10]$ zone axis. [(c) and (d)] FFT pattern obtained from the V_2O_3 film region and the Al_2O_3 substrate, respectively. (e) HAADF-STEM image of the 10 nm thick V_2O_3/Al_2O_3 heterostructure, and (f) the corresponding EDS elemental maps showing the distribution of aluminum (Al) and vanadium (V).

© Author(s) 2025

corresponding to the (0006) and $(11\bar{2}0)$ planes of V_2O_3, confirming the rhombohedral structure of V_2O_3. The substrate shows interplanar distances of 0.23 nm corresponding to the (0006) plane, confirming the rhombohedral structure of Al_2O_3. The FFT pattern of the film confirms that the growth direction aligns with the [0001] direction, consistent with the XRD result. These FFT patterns confirm the epitaxial growth of V_2O_3 thin film on Al_2O_3 substrate with the crystallographic relationship V_2O_3[0001]//Al_2O_3[0001]. Finally, no structural differences were detected between the near-interface region and far from it, as well as no traces of spurious phases or segregation of crystalline phases other than V_2O_3, while structural dislocations are mostly present at the film/substrate interface.

STEM experiments assisted by EDS analyses were also conducted to assess the chemical compositions of the thin film at the interface with the substrate and far from it. Figure 3(e) displays a representative HAADF STEM image of the V_2O_3/Al_2O_3 heterostructure along the $[\bar{1}10]$ zone axis. As the intensity of the HAADF STEM image is strongly dependent on the atomic number of the element, the obtained image exhibits distinct contrast, reflecting the different chemical composition: the bright layer corresponds to the V_2O_3 film, while the dark contrast refers to the Al_2O_3 substrate. The chemical composition for each species of interest (namely, Al and V) is obtained by collecting EDS spectra coupled with STEM. The EDS spectrum was collected perpendicular to the interface across the imaged region depicted in Fig. 3(e). Spatial elemental mapping reveals a homogeneous distribution of V (green) within the V_2O_3 film and Al (red) within the Al_2O_3 substrate [Fig. 3(f)]. In particular, EDS elemental profiles obtained across the region confirm that no Al interdiffusion into the V_2O_3 film can be ascertained, thus confirming the good chemical stability of the film/substrate interfacial region.

Strain distribution along the whole thickness of the V_2O_3 film was investigated by Geometrical Phase Analysis (GPA). In particular, GPA is capable of providing insight into crystal defects, heterostructures, and strain distributions in thin films by analyzing the periodic lattice fringes in high-resolution TEM (HRTEM) images (the HRTEM image presented in Fig. 4(a) was used for GPA analysis). However, unlike the common definition of ε_{xx} and ε_{zz} components of the strain tensor, which refer to the deformation in the relative change in shape or size of a material under investigation, in GPA analysis, both those quantities are referred to the substrate, which is chosen as a reference region as a strain-free baseline. In detail, the in-plane ε_{xx} and the out-of-plane ε_{zz} components of the strain tensor are calculated as $\varepsilon_{xx} = (a_{film} - a_{substrate})/a_{substrate}$ and $\varepsilon_{zz} = (c_{film} - c_{substrate})/c_{substrate}$, respectively ($a_{film}$ and $a_{substrate}$ are the in-plane lattice parameters of film and substrate, respectively, while c_{film} and $c_{substrate}$ refer to the out-of-plane lattice parameters). The technique applies Fourier transforms to identify phase shifts in the periodic lattice, allowing precise calculation of strain components. In detail, the two lattice periodicity spots $(11\bar{2}0)$ and (0001) in the diffractogram indicate the local Fourier components used to extract the corresponding in-plane and out-of-plane phase images,

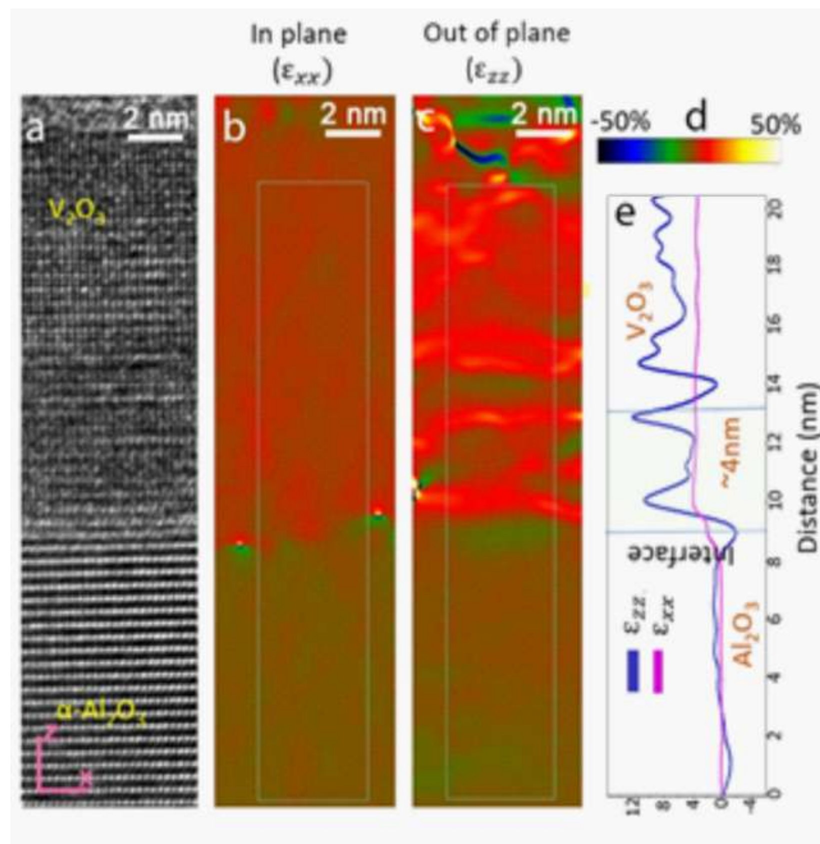

FIG. 4. (a) A HRTEM image of the interface between the V_2O_3 film of thickness 15 nm and Al_2O_3 substrate at high magnification. [(b) and (c)] In-plane and out-of-plane strain maps obtained from (a) using GPA, respectively. (d) Color bar corresponding to the strain maps. (e) Line profiles of the in-plane ε_{xx} (magenta) and out-of-plane ε_{zz} (blue) components of the strain tensor, averaged over the width of the strain maps, along the [110] direction of the film. All values are expressed as percentages.

22 August 2025 17:04:14

© Author(s) 2025

respectively. By analyzing the local Fourier components of the lattice fringes, the displacement fields in the HRTEM image were measured. Consequently, the phase image describes the position of the lattice fringes in real space with respect to the reference. The deformation map was, therefore, calculated by keeping the Al_2O_3 substrate as a reference lattice. By choosing the x-axis parallel to the interface and the z-axis along the perpendicular (growth) direction, ε_{xx} and ε_{zz} maps are presented in Figs. 4(b) and 4(c), respectively.

By analyzing the integrated line profiles of the strain distribution computed over the region marked in Fig. 4(b) and presented in Fig. 4(e), the in-plane strain component (ε_{xx}) exhibits a sharp increase from zero—corresponding to the undeformed substrate—to approximately +3.0% ± 0.5% within the first ~4 nm of the V_2O_3 film. This behavior is indicative of a rapid and nearly complete structural relaxation of the in-plane lattice parameter toward the bulk value of V_2O_3, which is around 4%. Notably, beyond this interfacial region, ε_{xx} remains essentially constant throughout the film thickness, suggesting that strain relaxation is confined to the initial nanometers of growth.

However, the evolution of the ε_{zz} out-of-plane component of the strain tensor is more complex [Fig. 4(c)]. Within the initial ~4 nm interfacial region, ε_{zz} displays significant fluctuations, indicating a highly disordered stacking of the out-of-plane lattice planes. Nevertheless, as the distance from the film/substrate interface increases, its value tends to a constant value close to its expected bulk-like value of about 7%, thus indicating the restoration of an ordered crystallographic structure. The whole set of results effectively demonstrates the presence of two distinct regions of the V_2O_3 thin film material: (i) a 4-nm wide interfacial region in which in-plane lattice registry of the film rapidly relaxes toward its bulk-like value while the out-of-plane lattice registry is characterized by a high structural disorder; and (ii) the complementary part of the film in which both ε_{xx} and ε_{zz} are substantially constant and equal to the expected value of fully relaxed V_2O_3. These observations underscore the importance of understanding the origin of such a structural disorder in the proximity of the film/substrate interface, which may critically influence the functional properties of the material.

In heteroepitaxial structures, lattice mismatch-induced strain is often alleviated through the formation of misfit dislocations (MDs) at the interface.[39–41] To elucidate the possible presence of MDs at the film/substrate interface as well as to fully explore their structural characteristics, HRTEM imaging was conducted at high magnification [Fig. 5(a)]. The resulting image was processed using the inverse fast Fourier transform (IFFT) technique to enhance visualization of the partially disordered local structure. Figure 5(b) displays the IFFT-filtered image of Fig. 5(a), highlighting reflections from the $(11\bar{2}0)$ and $(\bar{1}\bar{1}20)$ planes. The image reveals an array of MDs at the interface, with colored rectangular boxes marking extra half-planes within the film. The presence of these MDs indicates strain relaxation due to lattice misfit. To further investigate the MD regions, magnified views of dislocations from the HRTEM image are presented in Figs. 5(f)–5(h), with their corresponding IFFTs shown in Figs. 5(c)–5(e). The dislocation cores in Figs. 5(f)–5(h) appear

22 August 2025 17:04:14

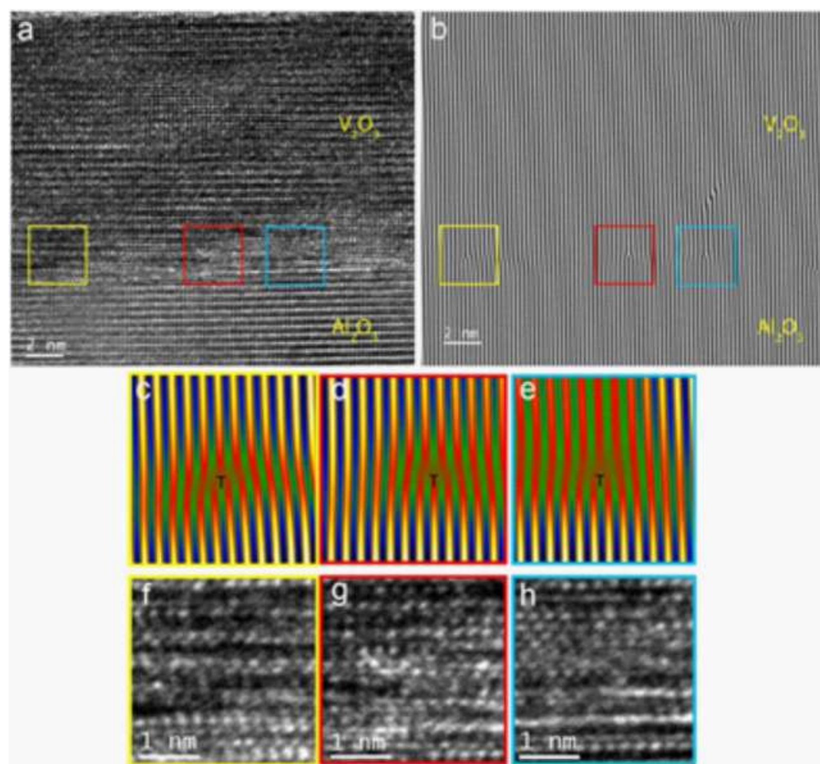

FIG. 5. (a) HRTEM image of the interface between a 15 nm thick V_2O_3 film and Al_2O_3 substrate. (b) The corresponding IFFT image obtained from an $(11\bar{2}0)$ Bragg reflection of the image. [(c)–(e)] IFFT images highlighting the region containing dislocations at higher magnification [(f)–(h)], corresponding HRTEM images with dislocations.

© Author(s) 2025

slightly blurred, likely due to the imaging direction, $[\bar{1}10]$, not being perfectly edge-on. The magnified IFFT images [Figs. 5(c)–5(e)] clearly show extra half-planes within the film, with dislocation cores marked. These extra half-planes in Al_2O_3 induce lattice distortion while maintaining equidistance between V_2O_3 atomic columns. Detailed IFFT analysis of the lattice images confirms the presence of edge dislocations at the interface, which play a critical role in strain relaxation between the film and substrate.[17]

III. CONCLUSION

In this study, we have investigated the structural properties of V_2O_3 thin films grown on sapphire Al_2O_3 substrate. XRD analysis revealed the in-plane orientations are V_2O_3 [0001]//Al_2O_3 [0001] and V_2O_3 $[10\bar{1}0]$//Al_2O_3 $[10\bar{1}0]$, as confirmed by the FFT pattern. HRTEM, HAADF-STEM, and EDS confirmed a chemically stable interface without detectable aluminum interdiffusion or secondary phase formation. GPA-based strain mapping revealed a localized strain confined within a ~4 nm interfacial region, attributed to large lattice mismatch and relieved via misfit dislocation formation. Beyond this strain-confined region, the film exhibits homogeneous structural characteristics and retains electronic properties—in particular, the valence state of vanadium and the crystal field environment—that are comparable to those of bulk V_2O_3, as discussed in our previous work.[23] This indicates that any changes in the MIT are predominantly due to dimensionality effects in thin films. This work paves the way for optimizing film-substrate interfaces in next-generation devices requiring precise control of strain and material properties.

IV. MATERIALS AND METHODS

A. Thin-film fabrication

Epitaxial V_2O_3 films were fabricated by the PLD technique, utilizing a fundamental harmonic Nd:YAG pulsed laser source (λ = 1064 nm, pulse width = 6–10 ns).[34,42] The typical beam size and laser energy of the unfocused beam are fixed at a diameter of 0.6 cm and an energy of 700 mJ, respectively. Upon focusing the laser beam onto the target, the resulting laser energy density is estimated to be ~20 J/cm^2. The substrate-to-target distance "*d*" was kept at 8 cm. The growth process was carried out at a substrate temperature of ~700 °C in ultrahigh vacuum conditions (background pressure during the growth process at high temperature was about 5×10^{-7} mbar). Subsequently, the films were cooled to room temperature under the same deposition pressure. The typical deposition rate of the film was about 3.5 Å/min, allowing full control over the film thickness. A series of films with nominal thicknesses of 5, 8, 10, and 15 nm were fabricated for this study.

B. X-ray diffraction characterization

The crystalline structure of the films was performed using a Malvern Empyrean four-circle x-ray diffractometer equipped with a double-bounce 2 × Ge(220) hybrid monochromator, providing a monochromatic $K_{\alpha 1}$ wavelength of 1.540 598 Å. The thickness and surface roughness of the films were measured with a parabolic mirror and a 0.27° parallel plate collimator. Reciprocal space maps were carried out by using a GaliPIX3D detector with a 481 × 465 pixel active window (corresponding to equatorial and axial sizes of 6.8898° and 5.7632°, respectively).

C. Scanning electron microscopy experiments

To examine the surface morphology of the V_2O_3 films, a Zeiss Supra 40 field-emission gun (FEG) Scanning Electron Microscope (SEM) was utilized. The SEM was equipped with a Gemini column and an in-lens detector, which enhanced the signal-to-noise ratio and improved imaging capabilities.

D. STEM Imaging

High-resolution transmission electron microscopy (HRTEM) and high-angle annular dark-field (HAADF) scanning TEM (STEM) investigations were conducted on cross-sectional samples by using a JEOL 2010 UHR field emission gun microscope operated at 200 kV. The microscope had a determined spherical aberration coefficient Cs of 0.47 ±0.01 mm. HAADF STEM images were acquired using an illumination angle of 12 mrad and a collection angle of $88 \leq 2\theta \leq 234$ mrad. In addition, the microscope is equipped with an Oxford system for energy-dispersive x-ray spectroscopy (EDS) studies. To determine the elemental chemical profiles across the interfacial region, EDS analyses were performed in STEM mode using a 0.5 nm electron probe.

Effective TEM characterization relies strongly on sample preparation techniques. In this study, initially, the sample was mechanically polished to refine its surface, followed by etching with an ion beam until perforation was achieved. The etching process was first set to a voltage of 3 kV and a current of 5 mA. Once the desired cavity formation had occurred, the ion-beam etching process continued at lower voltage and current to eliminate any debris generated during the process and achieve a clean area suitable for characterization.

E. Data evaluation

Gatan Digital Micrograph 3.13 (GMS 3.13) was employed to analyze the TEM image. To measure the strain within the film region, GPA developed by Hÿtch *et al.*[43] was utilized based on an HRTEM image. The strain map was calculated with scripts in the FRWR tools menu (FRWR, 2012)[44] integrated into the Gatan Digital Micrograph software. Two $[1\,1\,\bar{2}\,0]$ and [0001] Bragg spots were used to calculate two-dimensional symmetric strain components. The spatial sampling of the strain measurement was determined by the aperture size employed for the Bragg spots, resulting in a sampling resolution of 3 nm.

ACKNOWLEDGMENTS

This work was performed in the framework of the Nanoscience Foundry and Fine Analysis (NFFA-MUR Italy Progetti Internazionali) facility (www.trieste.nffa.eu). E. Cociancich is gratefully acknowledged for the TEM specimen preparation. PR and SPC acknowledge the receipt of a fellowship from the ICTP Program for Training and Research in Italian Laboratories, Trieste, Italy.

22 August 2025 17:04:14

© Author(s) 2025

AUTHOR DECLARATIONS

Conflict of Interest

The authors have no conflicts to disclose.

Author Contributions

P.R. and S.K.C. contributed equally to this work.

P. Rajak: Formal analysis (equal); Investigation (equal); Writing – original draft (equal); Writing – review & editing (equal). **S. K. Chaluvadi**: Formal analysis (equal); Investigation (equal); Validation (equal); Visualization (equal); Writing – original draft (equal); Writing – review & editing (equal). **S. Punathum Chalil**: Formal analysis (equal); Writing – review & editing (equal). **F. Mazzola**: Writing – review & editing (equal). **S. Passuti**: Investigation (equal); Writing – review & editing (equal). **P. Orgiani**: Supervision (equal); Validation (equal); Writing – original draft (equal); Writing – review & editing (equal). **G. Rossi**: Writing – review & editing (equal). **R. Ciancio**: Methodology (equal); Supervision (equal); Validation (equal); Writing – review & editing (equal).

DATA AVAILABILITY

The data that support the findings of this study are available from the corresponding author upon reasonable request.

REFERENCES

[1] R. Rousseau, V.-A. Glezakou, and A. Selloni, "Theoretical insights into the surface physics and chemistry of redox-active oxides," Nat. Rev. Mater. **5**, 460–475 (2020).

[2] P. Salev, J. del Valle, Y. Kalcheim, and I. K. Schuller, "Giant nonvolatile resistive switching in a Mott oxide and ferroelectric hybrid," Proc. Natl. Acad. Sci. U. S. A. **116**, 8798–8802 (2019).

[3] A. Ronchi, P. Franceschini, P. Homm, M. Gandolfi, G. Ferrini, S. Pagliara, F. Banfi, M. Menghini, J.-P. Locquet, and C. Giannetti, "Light-assisted resistance collapse in a V_2O_3-based Mott-insulator device," Phys. Rev. Appl. **15**, 044023 (2021).

[4] T. Nan, M. Liu, W. Ren, Z.-G. Ye, and N. X. Sun, "Voltage control of metal-insulator transition and non-volatile ferroelastic switching of resistance in VO_x/PMN-PT heterostructures," Sci. Rep. **4**, 5931 (2014).

[5] C. Müller, A. A. Nateprov, G. Obermeier, M. Klemm, R. Tidecks, A. Wixforth, and S. Horn, "Surface acoustic wave investigations of the metal-to-insulator transition of V_2O_3 thin films on lithium niobate," J. Appl. Phys. **98**, 084111 (2005).

[6] J. del Valle, P. Salev, F. Tesler, N. M. Vargas, Y. Kalcheim, P. Wang, J. Trastoy, M.-H. Lee, G. Kassabian, J. G. Ramírez, M. J. Rozenberg, and I. K. Schuller, "Subthreshold firing in Mott nanodevices," Nature **569**, 388–392 (2019).

[7] S. Wang, J. G. Ramírez, and I. K. Schuller, "Avalanches in vanadium sesquioxide nanodevices," Phys. Rev. B **92**, 085150 (2015).

[8] S. Sahoo, H. S. Kunwar, S. Yadav, R. Rawat, V. Sathe, D. M. Phase, and R. J. Choudhary, "Memristive thermal switching in epitaxial V_2O_3 thin film," J. Alloys Compd. **970**, 172620 (2024).

[9] S. Guénon, S. Scharinger, S. Wang, J. G. Ramírez, D. Koelle, R. Kleiner, and I. K. Schuller, "Electrical breakdown in a V_2O_3 device at the insulator-to-metal transition," Europhys. Lett. **101**, 57003 (2013).

[10] F. J. Morin, "Oxides which show a metal-to-insulator transition at the Neel temperature," Phys. Rev. Lett. **3**, 34–36 (1959).

[11] J. Jiang, L. Zhang, Y. Hu, Y. Guo, Z. Chen, R. Jia, S. Pendse, Y. Xiang, G.-C. Wang, Y. Shi, and J. Shi, "Metal–insulator transition of single-crystal V_2O_3 through van der Waals interface engineering," ACS Nano **17**, 11783–11793 (2023).

[12] M. Yethiraj, "Pure and doped vanadium sesquioxide: A brief experimental review," J. Solid State Chem. **88**, 53–69 (1990).

[13] D. B. McWhan, A. Menth, J. P. Remeika, W. F. Brinkman, and T. M. Rice, "Metal-insulator transitions in pure and doped V_2O_3," Phys. Rev. B **7**, 1920–1931 (1973).

[14] D. B. McWhan, J. P. Remeika, T. M. Rice, W. F. Brinkman, J. P. Maita, and A. Menth, "Electronic specific heat of metallic Ti-doped V_2O_3," Phys. Rev. Lett. **27**, 941–943 (1971).

[15] P. D. Dernier and M. Marezio, "Crystal structure of the low-temperature antiferromagnetic phase of V_2O_3," Phys. Rev. B **2**, 3771–3776 (1970).

[16] C. Grygiel, C. Simon, B. Mercey, W. Prellier, R. Frésard, and P. Limelette, "Thickness dependence of the electronic properties in V_2O_3 thin films," Appl. Phys. Lett. **91**, 262103 (2007).

[17] L. Dillemans, T. Smets, R. R. Lieten, M. Menghini, C.-Y. Su, and J.-P. Locquet, "Evidence of the metal-insulator transition in ultrathin unstrained V_2O_3 thin films," Appl. Phys. Lett. **104**, 071902 (2014).

[18] M. Copel, M. A. Kuroda, M. S. Gordon, X.-H. Liu, S. S. Mahajan, G. J. Martyna, N. Moumen, C. Armstrong, S. M. Rossnagel, T. M. Shaw, P. M. Solomon, T. N. Theis, J. J. Yurkas, Y. Zhu, and D. M. Newns, "Giant piezoresistive on/off ratios in rare-earth chalcogenide thin films enabling nanomechanical switching," Nano Lett. **13**, 4650–4653 (2013).

[19] Y. Zhou and S. Ramanathan, "Correlated electron materials and field effect transistors for logic: A review," Crit. Rev. Solid State Mater. Sci. **38**, 286–317 (2013).

[20] E. B. Thorsteinsson, S. Shayestehaminzadeh, and U. B. Arnalds, "Tuning metal-insulator transitions in epitaxial V_2O_3 thin films," Appl. Phys. Lett. **112**, 161902 (2018).

[21] J.-H. Ha, H.-W. Kim, Y.-S. Jo, S.-W. Kim, and J.-I. Hong, "Tunable metal-insulator transition of V_2O_3 thin films strained by controlled inclusion of crystallographic defect," Appl. Mater. Today **22**, 100984 (2021).

[22] J. G. Ramirez, T. Saerbeck, S. Wang, J. Trastoy, M. Malnou, J. Lesueur, J.-P. Crocombette, J. E. Villegas, and I. K. Schuller, "Effect of disorder on the metal-insulator transition of vanadium oxides: Local versus global effects," Phys. Rev. B **91**, 205123 (2015).

[23] V. Polewczyk, S. K. Chaluvadi, D. Dagur, F. Mazzola, S. Punathum Chalil, A. Y. Petrov, J. Fujii, G. Panaccione, G. Rossi, P. Orgiani, G. Vinai, and P. Torelli, "Chemical, structural and electronic properties of ultrathin V_2O_3 films on Al_2O_3 substrate: Implications in Mott-like transitions," Appl. Surf. Sci. **610**, 155462 (2023).

[24] A. Vittadini, M. Casarin, M. Sambi, and A. Selloni, "First-principles studies of vanadia–titania catalysts: Beyond the Monolmyer," J. Phys. Chem. B **109**, 21766–21771 (2005).

[25] A. Vittadini and A. Selloni, "Periodic density functional theory studies of vanadia−titania catalysts: Structure and Stabisity of the Oxidioed Monolmyer," J. Phys. Chem. B **108**, 7337–7343 (2004).

[26] F. Mazzola, S. K. Chaluvadi, V. Polewczyk, D. Mondal, J. Fujii, P. Rajak, M. Islam, R. Ciancio, L. Barba, M. Fabrizio, G. Rossi, P. Orgiani, and I. Vobornik, "Disentangling structural and electronic properties in V_2O_3 thin films: A genuine nonsymmetry breaking Mott transition," Nano Lett. **22**, 5990–5996 (2022).

[27] A. S. McLeod, E. van Heumen, J. G. Ramirez, S. Wang, T. Saerbeck, S. Guenon, M. Goldflam, L. Anderegg, P. Kelly, A. Mueller, M. K. Liu, I. K. Schuller, and D. N. Basov, "Nanotextured phase coexistence in the correlated insulator V_2O_3," Nat. Phys. **13**, 80–86 (2017).

[28] T. Saerbeck, J. de la Venta, S. Wang, J. G. Ramírez, M. Erekhinsky, I. Valmianski, and I. K. Schuller, "Coupling of magnetism and structural phase transitions by interfacial strain," J. Mater. Res. **29**, 2353–2365 (2014).

[29] K. Manjunath, R. Singh, D. P. Panda, and C. N. R. Rao, "Metal–insulator transitions in stable V_2O_3 thin films: Atomic layer deposition and postdeposition annealing studies," Phys. Status Solidi RRL **15**, 2000565 (2021).

[30] P. Homm, M. Menghini, J. W. Seo, S. Peters, and J. P. Locquet, "Room temperature Mott metal–insulator transition in V_2O_3 compounds induced via strain-engineering," APL Mater. **9**, 021116 (2021).

[31] L. Dillemans, R. R. Lieten, M. Menghini, T. Smets, J. W. Seo, and J.-P. Locquet, "Correlation between strain and the metal–insulator transition in epitaxial V_2O_3 thin films grown by molecular beam epitaxy," Thin Solid Films **520**, 4730–4733 (2012).

22 August 2025 17:04:14

© Author(s) 2025

[32] I. Mjejri, A. Rougier, and M. Gaudon, "Low-cost and facile synthesis of the vanadium oxides V_2O_3, VO_2, and V_2O_5 and their magnetic, thermochromic and electrochromic properties," Inorg. Chem. **56**, 1734–1741 (2017).
[33] M. Caputo, J. Jandke, E. Cappelli, S. K. Chaluvadi, E. Bonini Guedes, M. Naamneh, G. Vinai, J. Fujii, P. Torelli, I. Vobornik, A. Goldoni, P. Orgiani, F. Baumberger, M. Radovic, and G. Panaccione, "Metal to insulator transition at the surface of V_2O_3 thin films: An in-situ view," Appl. Surf. Sci. **574**, 151608 (2022).
[34] P. Orgiani, S. K. Chaluvadi, S. P. Chalil, F. Mazzola, A. Jana, S. Dolabella, P. Rajak, M. Ferrara, D. Benedetti, A. Fondacaro, F. Salvador, R. Ciancio, J. Fujii, G. Panaccione, I. Vobornik, and G. Rossi, "Dual pulsed laser deposition system for the growth of complex materials and heterostructures," Rev. Sci. Instrum. **94**, 033903 (2023).
[35] P. Rajak, D. Knez, S. K. Chaluvadi, P. Orgiani, G. Rossi, L. Méchin, and R. Ciancio, "Evidence of Mn-ion structural displacements correlated with oxygen vacancies in $La_{0.7}Sr_{0.3}MnO_3$ interfacial dead layers," ACS Appl. Mater. Interfaces **13**, 55666–55675 (2021).
[36] P. Rajak, R. Ciancio, A. Caretta, S. Laterza, R. Bhardwaj, M. Jugovac, M. Malvestuto, P. Moras, and R. Flammini, "Evidence of silicide at the Ni/β-Si_3N_4(0001)/Si(111) interface," Appl. Surf. Sci. **623**, 156986 (2023).
[37] W. R. Robinson, "High-temperature crystal chemistry of V_2O_3 and 1% chromium-doped V_2O_3," Acta Crystallogr., Sect. B **31**, 1153–1160 (1975).
[38] L. Lutterotti and P. Scardi, "Simultaneous structure and size–strain refinement by the rietveld method," J. Appl. Crystallogr. **23**, 246–252 (1990).
[39] C. Marzano and P. P. Dholabhai, "High-throughput prediction of thermodynamic stabilities of dopant-defect clusters at misfit dislocations in perovskite oxide heterostructures," J. Phys. Chem. C **127**, 15988–15999 (2023).
[40] F. Sandiumenge, "A multiscale perspective on misfit dislocations in oxide films," Front. Mater. **6**, 1–6 (2019).
[41] I. J. Beyerlein, M. J. Demkowicz, A. Misra, and B. P. Uberuaga, "Defect-interface interactions," Prog. Mater. Sci. **74**, 125–210 (2015).
[42] S. K. Chaluvadi, D. Mondal, C. Bigi, D. Knez, P. Rajak, R. Ciancio, J. Fujii, G. Panaccione, I. Vobornik, G. Rossi, and P. Orgiani, "Pulsed laser deposition of oxide and metallic thin films by means of Nd:YAG laser source operating at its 1st harmonics: Recent approaches and advances," J. Phys.: Mater. **4**, 032001 (2021).
[43] M. J. Hÿtch, E. Snoeck, and R. Kilaas, "Quantitative measurement of displacement and strain fields from HREM micrographs," Ultramicroscopy **74**, 131–146 (1998).
[44] C. T. Koch, "Determination of core structure periodicity and point defect density along dislocations," Ph.D. thesis, Arizona State University, 2002.

22 August 2025 17:04:14

© Author(s) 2025